Journal of Materials Chemistry A

Accepted Manuscript

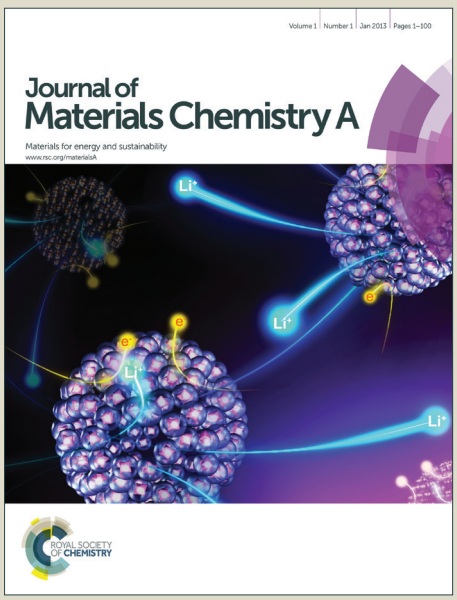

ROYAL SOCIETY OF CHEMISTRY

www.rsc.org/materialsA

Journal Name

RSCPublishing

ARTICLE

Synthesis of Self-Stacked $CuFe_2O_4$-Fe_2O_3 Porous Nanosheets as High Performance Li-Ion Battery Anode

Cite this: DOI: 10.1039/xoxxoooooox

Fei-Xiang Ma,[a,b] Pan-Pan Wang,[a,b] Cheng-Yan Xu,[a,b,*] Jing Yu,[a,b] Hai-Tao Fang[a] and Liang Zhen[a,b,*]

Received ooth January 2012,
Accepted ooth January 2012

DOI: 10.1039/xoxxoooooox

www.rsc.org/

Self-stacked $CuFe_2O_4$-Fe_2O_3 porous nanosheets were prepared via a facile polyol-mediated route followed by calcination. Benefited from its highly porous structures and good electrical and ion conductivity of the well-dispersed $CuFe_2O_4$ phase in the matrix, the hybrid material exhibits high specific capacity of 910 mA h g^{-1} at 0.5 C after 200 cycles, superior capacity retention (0.02 % capacity loss per cycle) and good rate capability (417 mA h g^{-1} at 4 C) as a promising anode material for Li-ion batteries.

1. Introduction

Li-ion batteries (LIBs) with high energy and power densities are highly demanded to power the next generation electric vehicles and stationary generation[1-3]. Unfortunately, current commercial graphite anode, with low theoretical capacity of 372 mA h g^{-1}, greatly limits the further development of LIBs, which urges people to continually search for new anode materials with high capacities and long cycle life to meet the growing device demand. Considered as advanced anodes of Li-ion battery since 2000[4], transition metal oxides (TMOs) including CuO[5], NiO[6], Co_3O_4[7], Fe_3O_4[8], MnO[9] as well as their binary oxides[10-13], based on their conversion reaction with Li-ions, have attracted tremendous attention because of their large specific capacities up to 1000 mA h g^{-1},[14] about three times greater than that of commercial graphite. Among these TMOs, Fe_2O_3 has been considered as a promising anode material because of its high theoretical specific capacity of 1007 mA h g^{-1}, assuming 6 moles of Li uptake/extraction per formula unit, derived from the reversible conversion reaction: $Fe_2O_3 + 6Li \leftrightarrow 3Li_2O + Fe$[15-17], low cost and environmental abundance and benignity. However, analogy to other TMOs, Fe_2O_3 suffers from serious kinetic problems derived from its intrinsically low electrical conductivity and slow solid-state diffusion of Li-ions, which make it rather difficult to fully utilize the conversion reaction and result in limited rate capabilities in practice[14, 18]. Moreover, dramatic volume changes (~90%) during repetitive cycling reactions between Fe_2O_3 and Li ions may result in anode pulverization and decrease of electrical connectivity, leading to a rapid decline in capacity and poor cycling stability[19].

To overcome these problems, downsize Fe_2O_3 particles to nanoscale[18, 20-21] and design/engineering various porous Fe_2O_3 structures, such as hollow or porous spheres[22,23], microboxs[24], hierarchical structures[25,26] mesoporous nanospindle[27] and nanotubes[28], have been proved to be effective strategies to not only mitigate the effect of volume change but also enhance Li-ion transfer ability during lithium cycling for improving their cycle performance. However, their intrinsic electrical conductivity, another essential factor that determines the electrochemical performance, has not yet change in such nanostructures. Thus, most reported bare Fe_2O_3 nanostructures exhibit unsatisfied cycle stabilities and rate capabilities. In this regard, various carbon-based additives, such as amorphous carbon[29,30], carbon nanotubes (CNTs)[31,32] and graphene[33,34], have been mixed with high capacity Fe_2O_3 nanomaterials for improving their electrical contact and structure stability during cycling. Feng's group[34] developed a facile refluxing procedure to synthesize porous Fe_2O_3 nanobelts/graphene composite, which delivery a ultrahigh reversible capacity of 1046 mA h g^{-1} and maintain nearly 100% capacity after 130 cycles for lithium storage. Fe_2O_3 nanoparticles can be confined into carbon nanotubes to form a hybrid structures with improved electrochemical performance in terms of high reversible capacity, excellent cycling stability (811 mA h g^{-1} after 100 cycles) and high rate capability[32]. Coating amorphous carbon on Fe_2O_3 nanoparticles was also applied to improve electrochemical properties of Fe_2O_3 nanostructures. Lou's group[31] successfully prepared carbon-coated Fe_2O_3 hollow nanohorns on the CNT backbone with superior lithium storage capabilities. Fan's group[35] fabricated Fe_2O_3/C nanofibers using a simple electrospinning technology, which display satisfied capacity retention. However, high content of the electrochemical active carbon in the composite materials may result in lower specific capacities than the theoretical capacity of Fe_2O_3. Thus, novel porous structures, combined with active

materials with high electrical conductivity and high capacity, are highly desired to improving the electrochemical performance of Fe_2O_3 electrode. Recently, doping of metal oxide nanostructures with various other transition metal ions, dramatically increasing their inherent conductivities with several orders, has been proved to be an effective approach to promote the electrochemical properties of the anode materials.[13, 36-38] Therefore, design and synthesis of doped Fe_2O_3 materials with highly porous nanostructures should be a highly desired route to enhance the electrochemical properties of Fe_2O_3 nanomaterials.

Herein, we successfully prepared self-stacked $CuFe_2O_4$-Fe_2O_3 porous nanosheets through a simple polyol-mediated refluxing route combined with thermal annealing in air. The unique hierarchical architecture assembled by porous nanosheets greatly enhances the facility of electrolyte penetration, and the high conductivity of $CuFe_2O_4$ is beneficial for the fast transfer of electrons and ions. As an anode material of LIBs, the as-synthesized self-stacked $CuFe_2O_4$-Fe_2O_3 porous nanosheets manifest an impressive electrochemical property with high specific capacity and cycle stability at high charge-discharge currents.

2. Experimental

2.1 Materials synthesis

$FeCl_3 \cdot 6H_2O$, copper (II) acetate monohydrate ($Cu(Ac)_2 \cdot H_2O$) sodium acetate anhydrous (NaAc) and ethylene glycol (EG) were purchased from Sinopharm Chemical Reagent Co., Ltd, and used without further purification. In a typical synthesis of self-stacked CuFe-glycolate nanosheet precursor, 2 mmol $FeCl_3 \cdot 6H_2O$ (~ 0.54 g) and 3 mmol $Cu(Ac)_2 \cdot H_2O$ (~ 0.6 g) were dissolved in EG (40 ml) in a 100 ml three-necked flask equipped with a reflux condenser and Teflon-coated magnetic stir bar. Then the reaction mixtures were heated to 150°C at an approximately 15 °C/min heating rate and allowed to heat for 60 min. Finally, the product was collected by centrifugation followed by repeated washing with ethanol for several times, and then dried in an oven at 60°C overnight. Finally, the as-prepared precursors were calcined in air at 350°C for 3 h with a heating rate of 2 °C/min.

2.2 Characterization

X-ray diffraction (XRD) patterns were collected using a Rigaku D/Max-γB diffractometer with Cu K_α radiation. The morphology and structure of the products were characterized by using a field-emission scanning electron microscope (FE-SEM, FEI Quanta 200F) equipped with an energy-dispersive X-ray spectrometer (EDS), and a transmission electron microscope (TEM, JEOL JEM-2100) with an accelerating voltage of 200 kV. X-ray photo-electron spectrometry (XPS) of the product was obtained on a VG K_α Probe spectrometer (Thermo Fisher Scientific) with Al K_α radiation as the excitation source. The thermal analysis was determined by SDT Q600 (TA Instruments) under air atmosphere at a heating rate of 10 °C/ min from room temperature to 800°C. Nitrogen adsorption-desorption was determined by Brunauer-Emmett-Teller (BET) tests using a Micromeritics ASAP 2020 system.

2.3 Electrochemical measurements

Electrochemical measurements were performed with Land-CT2001A battery test system (Jinnuo Wuhan Corp., China) by assembly of 2025 coin-type cells. Working electrodes were prepared by pasting a mixture of active materials, super P and sodium carboxymethyl cellulose (CMC) with a weight ratio of 70:20:10 onto a copper foil. After drying, the foil was punched into circular discs with 1.54 cm^{-2} active surface area. Then the electrode was pressed under 10 MPa pressure for 5 min and dried in vacuum at 80°C for 10 h before assembling the coin cells in an argon-filled glovebox (Mbraun, Unilab, Germany). The typical loading density of the active material was approximately 1.3 mg/cm^2. The electrolyte was composed of 1 M $LiPF_6$ solution in ethylene carbonate (EC)/dimethyl carbonate (DMC) /ethyl methyl carbonate (EMC) mixture solution (1:1:1 by volume). The lithium metal and Celgard 2400 (Celgard polypropylene) were employed as anode and separator, respectively. Cyclic voltammetry (CV) measurement and electrochemical impedance spectroscope (EIS) measurements were carried out on a CHI660E electrochemical workstation (Shanghai Chenhua Instrument Corp., China).

3. Results and discussion

The low-magnification FE-SEM image of CuFe-glycolate precursor (Fig. 1a) revealed unique, yet uniform self-stacked architecture with length of approximately 8 μm and width of about 4 μm. The building blocks were smooth nanosheets (Fig. 1b). The side edges of the nanosheets with thickness of ca. 50 nm can be clearly seen in Fig. 1c. Obvious spaces between the neighbouring nanosheets can be also observed from the side view. The compositions of the as-prepared precursor were investigated using EDS analysis (Fig. S1†). The Cu:Fe element ratio of the precursor was approximately 1:4.4, which was far deviated from the original Cu:Fe element ratio (3:2). In our reaction system, $Cu(Ac)_2$ played two roles, alkaline source for $FeCl_3$ hydrolysis and reaction agent with EG. Partial Cl^- of $FeCl_3$ might exchange with Ac^- in the $Cu(Ac)_2$ to form $Fe(Ac)_xCl_{3-x}$, and then the as-formed $Fe(Ac)_xCl_{3-x}$ and residual $Cu(Ac)_2$ can react together with EG to generate CuFe-glycolate precursor. However, without adding $Cu(Ac)_2 \cdot H_2O$ or replace $Cu(Ac)_2 \cdot H_2O$ with H_2O, no precipitation can be obtained, which further illustrated the occurrence of ion-exchange reaction between Fe^{3+} and Cu^{2+}. If 3 mmol $Cu(Ac)_2 \cdot H_2O$ was replaced with 6 mmol NaAc, irregular nanoparticles with a broad size distribution were generated (Fig. S2†), suggesting that $Cu(Ac)_2 \cdot H_2O$ also affected the morphology of precusor.

XRD and FTIR analysis were used to confirm the formation of CuFe-glycolate precursor. XRD pattern of as-synthesized CuFe-glycolate precursor was shown in Fig. S3a†. An strongest diffraction peak at around 10.5º, similar to those of Zn-glycolate, Co-glycolate, Ce-glycolate and Fe-glycolate, was detected, illustating the formation of CuFe-glycolate phase.

FTIR analysis was also performed to identify the functional groups on the surface of the CuFe-glycolate precursor, as shown in Fig. S3b†. A broad band around 3300 cm^{-1} indicated –OH stretching mode, ascibed to the unreacted traces of glycols. Some characteristic bands including the C–H stretching vibrations located around 2907 cm^{-1} and 2839 cm^{-1} and the C–O stretching at around 1100 cm^{-1} indicated the existence of glycol molecules. Band around 1636 cm^{-1} can be ascribed to the H–O–H bending vibration mode of phsically adsorbed water molecules[11, 39]. Based on the above XRD and FTIR analysis, metal-glycolate structures were sucessfully generated in the polyol refluxing process. In addition, the precursor prepared with NaAc as the additive was Fe-glycolate, as revealed from the XRD pattern with a stronggest diffracion peak at about 11° (Fig. S4†).

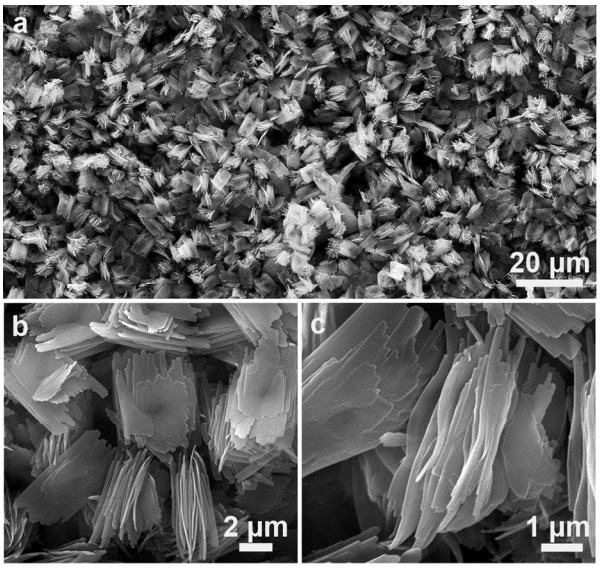

Fig. 1 Typical SEM images of as-synthesized CuFe-glycolate precursor at different magnifications.

In order to rationally determine the calcination temperature of the as-prepared CuFe-glycolate precursor, TGA/DSC was also performed. Fig. S5† showed the TGA/DSC curve recorded by heating the dry powder of precursor in air from room temperature to 800°C. A noticeable weight loss stage beginning from room temperature to 300°C with a sharp exothermic peak at 260°C from the DSC curve can be observed in the TG curve of the precursor, which can be ascribed to the formation of crystalline $CuFe_2O_4$-Fe_2O_3 phase through decomposition of the CuFe-glycolate precursor.

On the basis of the above TGA/DSC result, the calcination temperature was set at 350°C to convert the precursor to crystalline metal oxide completely. XRD pattern of the self-stacked $CuFe_2O_4$-Fe_2O_3 porous nanosheets, recorded after thermal annealing at 350°C for 3 h in air, was shown in Fig. 2. The parttern fits well with the rhombohedral Fe_2O_3 (JCPDS no. 33-0664) and cubic $CuFe_2O_4$ (JCPDS no. 25-0283) phases. No peaks from other crystalline impurities can be identified.

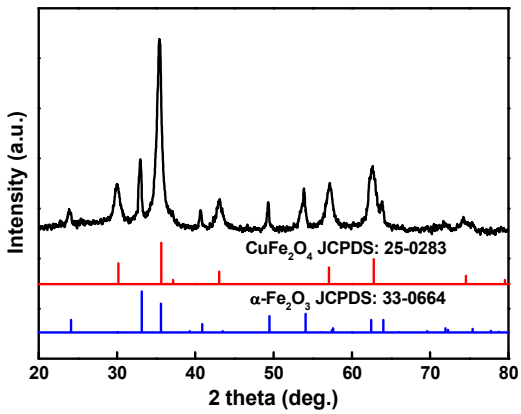

Fig. 2 XRD pattern of as-prepared $CuFe_2O_4$-Fe_2O_3 nanosheets.

XPS analysis was conducted to obtain the further information about the chemical compositions and chemical bonding state of $CuFe_2O_4$-Fe_2O_3 sample, and the results were shown in Fig. 3. The survery spectrum (Fig. 3a) confirmed the existence of Cu, Fe and O. The high-resolution region scan spectra for Cu 2p (Fig. 3b) displayed binding energy peaks of $2p_{3/2}$ and $2p_{1/2}$ at 934.1 eV and 954.1 eV, indicating that copper was in the +2 oxidation state[36, 40]. Likewise, the high-resolution high-resolution spectrum for Fe 2p (Fig. 3c) in the sample revealed Fe $2p_{3/2}$ and Fe $2p_{1/2}$ binding energy peaks at 711.1 eV and 724.8 eV, respectively with a energy difference of 13.7 eV, which were characteristic of iron in its +3 oxidation state[40-41]. In addition, an obvious satellite peak at 719.2 eV in Fig. 3c was characteristic of α-Fe_2O_3[41]. Therefore, combined with the XRD and XPS analysis, we can conclude that mixed $CuFe_2O_4$-Fe_2O_3 phases were indeed formed after calcination of the CuFe-glycolate precursor.

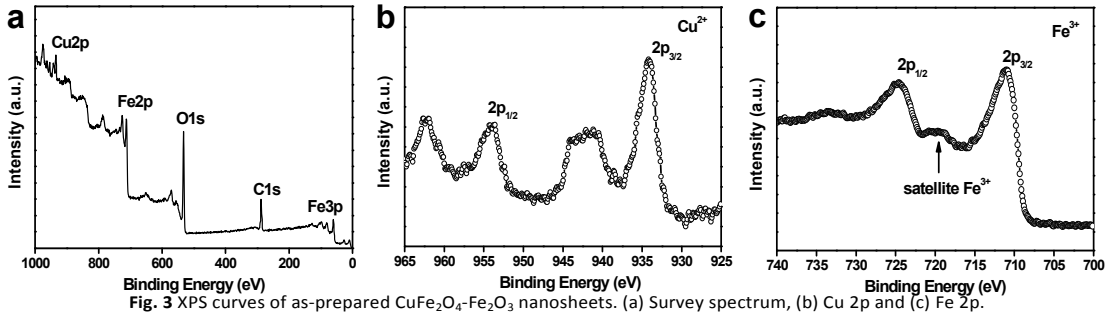

Fig. 3 XPS curves of as-prepared $CuFe_2O_4$-Fe_2O_3 nanosheets. (a) Survey spectrum, (b) Cu 2p and (c) Fe 2p.

Journal Name RSCPublishing

ARTICLE

SEM and TEM were used to reveal the morphological and structural details of the obtained self-stacked $CuFe_2O_4$-Fe_2O_3 nanosheets. Similar with the sheet-like morphology of the pristine CuFe-glycolate precursor, the self-stacked hierarchical architecture were well maintained with size unchanged after thermal annealing, as shown in Fig. 4a. Slightly carved nanosheets, caused by the existence of uneven stress during the calcination, can also be found (Fig. 4b). Mesoporous nanosheets composed of nano-sized primary particles generated through the decomposition of organic agent existed in CuFe-glycolate precursor can be clearly observed in the high-magnification SEM image (Fig. 4c). EDS result (Fig. S6†) showed that the Cu:Fe element ratio of the calcined product was 1:5. Based on the Cu:Fe element ratio of the calcined product, the $CuFe_2O_4$ and Fe_2O_3 phase ratio was estimated to 2:3. Element mapping images of a single self-stacked $CuFe_2O_4$-Fe_2O_3 porous nanosheet (Fig. S7†) showed the homogeneous distributions of all the three elements (Cu, Fe, and O) existed in the sample, suggesting the $CuFe_2O_4$ and Fe_2O_3 nanocrystals were uniformly distributed in the porous nanosheet matrix. As for Fe-glycolate precursor nanoparticles, their post-annealing product can be identified to rhombohedral Fe_2O_3 (JCPDS no. 33-0664) (Fig. S8†), and their annealing morphology was found to be severely aggregate and irregular nanoparticles (Fig. S9†).

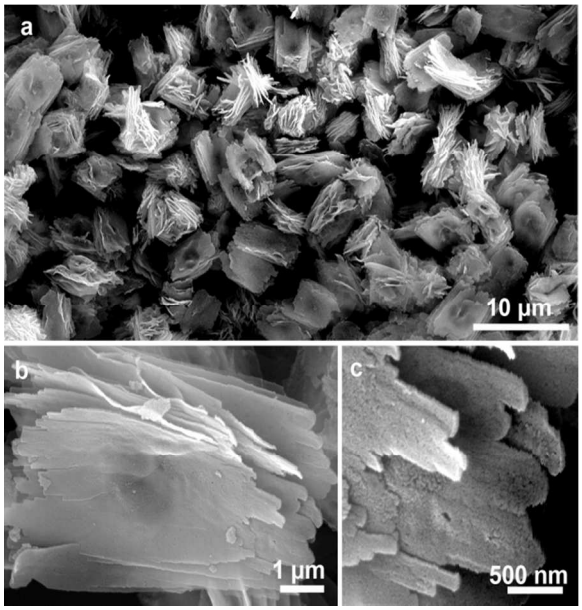

Fig. 4 Typical FE-SEM images of as-synthesized $CuFe_2O_4$-Fe_2O_3 nanosheets after annealing at 350°C for 3 h in air.

Further insight into the morphology and microstructure (Fig. 5 and Fig. S10†) of the self-stacked $CuFe_2O_4$-Fe_2O_3 porous nanosheets was gained by using TEM, HRTEM and SAED. Fig. 5a showed a typical TEM image of as-synthesized $CuFe_2O_4$-Fe_2O_3 nanosheets, which revealed their highly porous structures. The corresponding SAED pattern of Fig. 5a was shown in Fig. S10a†. It is obvious that the hierarchical structure is poly-crystalline in nature. High-magnification TEM image (Fig. 5b), taken from the edge of $CuFe_2O_4$-Fe_2O_3 porous nanosheets, clearly demonstrated that many tiny nanoparticles with size of ~5 to 25 nm were connected together and well dispersed in the porous nanosheets, and the size of the pores among nanocrystals was estimated to be ca. 10 nm. HRTEM image (Fig. S10b†) taken from the edge of this nanosheet revealed that $CuFe_2O_4$ and Fe_2O_3 nanoparticles connected together. During the decomposition of the CuFe-glycolate precursor, the spontaneous phase separation process originated from the possible Cu ion diffusion behavior was suggested to form $CuFe_2O_4$-Fe_2O_3 nanocrystal based porous nanosheets.

In order to reveal the formation mechanism of $CuFe_2O_4$-Fe_2O_3 porous nanosheets, we checked the morphology of intermediate product of the precursor nanosheets. It was interesting to find that the intermediate product at a short reaction of only 30 min possessed nanosheet-like characteristics (Fig. S11†), similar to that of the final product. The lengths and widths of intermediate nanosheets were comparable to that of the final product, while the thicknesses were rather small (corresponding to appreciate 1~3 layers). Therefore, the possible formation processes of the self-stacked CuFe-glycolate precursor nanosheets could be described as follows: single layer nanosheet firstly emerged because of the laminar structure of the CuFe-glycolate precursor and the subsequent grown CuFe-glycolate precursor nanoparticles grown on the nanosheets to form a second layer nanosheet. As a result, many layers nanosheets were stacked together to form three dimensional hierarchical structures as the reaction preceded.

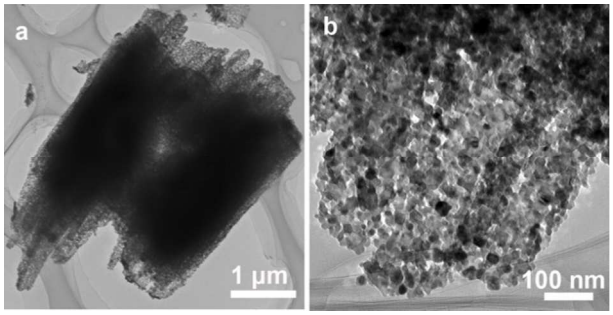

Fig. 5 Typical TEM images of as-synthesized $CuFe_2O_4$-Fe_2O_3 nanosheets after thermal annealing at 350°C for 3 h in air.

The nitrogen adsorption-desorption isotherm and corresponding BJH desorption pore size distribution of the calcined product were shown in Fig. 6. The BET surface area was determined to be about 62.5 m^2 g^{-1} for the $CuFe_2O_4$-Fe_2O_3 porous nanosheets. The BJH pore size distribution (inset in Fig. 6) calculated from adsorption branches demonstrated the presence of bimodal porosity: 10.9 nm mesopores (2–50 nm) may be derived from the decomposition of organic agent existed in the CuFe-glycolate precursor, and 83.4 nm macropores (>50 nm) might be generated from the self-stacked architecture, including the presence of interface space between the neighbour nanosheets. When evaluated as an anode material for LIBs, the identified porosity and highly open architecture should be helpful for quickly accessing the electrolyte solution and accommodating the serious volume change, widely presented in the conversion reaction based metal oxide electrodes, during the repeated cycling[14, 42-43]. In addition, the high conductivity of $CuFe_2O_4$ phase might be useful to further enhance the rate capability.

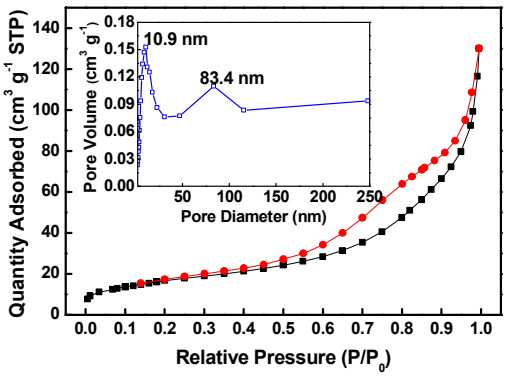

Fig. 6 N_2 adsorption-desorption isotherms of as-prepared porous $CuFe_2O_4$-Fe_2O_3 nanosheets, inset is the corresponding pore size distribution derived from the desorption isotherm.

Fig. 7 showed the electrochemical properties of the self-stacked $CuFe_2O_4$-Fe_2O_3 porous nanosheets produced via the feasible and cost-effective two-step strategy, namely, preparing CuFe-glycolate precursor nanosheets firstly followed by calcination. The electrochemical properties of the as-prepared Fe_2O_3 nanoparticles were also investigated to illustrate the excellent properties of the self-stacked $CuFe_2O_4$-Fe_2O_3 porous nanosheets. The cyclic voltammograms (CVs) of the initial three cycles were recorded at a slow scanning rate of 0.1 mV s^{-1} within the potential window of 0.01–3 V versus Li/Li^+ (Fig. 7a). In the first discharge curve, the small peak located at 0.85 V can be assigned to the formation of stable intermediate $Li_nCuFe_2O_4$[44] and $Li_nFe_2O_3$[35] phase. The following well-defined sharp peak around 0.55 V corresponds to the electrochemical reduction of Cu^{2+}/Fe^{3+} to Cu^0 and Fe^0[23, 35], as well as the formation of amorphous Li_2O and the irreversible decomposition of the solvent in the electrolyte to form solid electrolyte interphase (SEI). During the subsequent cathodic scans, an obvious peak shifting from ca. 0.55 V to ca. 0.8 V occurred, revealing the minor structure rearrangement, drastic lithium driven, structural or textural modifications happened on active material. The broader peak in the range of 1.6–1.8 V in the anodic scan curves could be ascribed to the oxidation of Cu and Fe metal nanoparticles to the metal oxides CuO and Fe_2O_3, and to possible decomposition of the as-formed SEI[44-45]. In the subsequent two discharge-charge curves, the profiles of the CV curves of the second and third cycle were well overlapped, indicating the highly reversible lithium insertion/desertion behavior. Fig. 7b showed the representative discharge-charge voltage profiles of the $CuFe_2O_4$-Fe_2O_3 electrode over a current density of 500 mA g^{-1} within a cutoff voltage window of 0.01–3 V. Two voltage plateaus at 0.75 and 0.9 V during the first discharge can be clearly identified, consistent well with the above CVs discussion (0.75 V vs 0.55 V). As shown in Fig. 7b, the initial discharge and charge capacity of the $CuFe_2O_4$-Fe_2O_3 electrode reached 1307 mA h g^{-1} and 972 mA h g^{-1}, respectively, corresponding to an initial irreversible capacity loss of 29%. The relatively high initial capacity loss can be mainly ascribed to the formation of SEI, which is very common in the transition metal oxide based electrode materials[7, 13, 14, 22]. After initial conditioning cycles, the Coulombic efficiency (CE) increased to more than 98%, indicating that the formed surface of SEI film retained intact and the electrochemical reactions were well reversible[46-47]. The cycling performances of the $CuFe_2O_4$-Fe_2O_3 and Fe_2O_3 electrodes cycled between 0.01 V and 3 V at constant current density of 500 mA g^{-1} were presented in Fig. 7c. The capacity of $CuFe_2O_4$-Fe_2O_3 electrode showed a sluggish decrease during the first 75 cycles followed by a slow increase in the subsequent steps, which is a general phenomenon in the metal oxide based anode electrode. Initial capacity fading occurred first due to mechanical degradation and unstable SEI formation on cycling, and subsequent gradual increase of the capacity might be attributed to the structure refinement to more stable structures[48] and the reversible growth of the gel-like polymer layer that wrapped the nanoparticles of the electrode[49, 50]. After 200 cycles, the discharge capacity of the $CuFe_2O_4$-Fe_2O_3 electrode maintained as high as 928 mA h g^{-1}, which was about 2.5 times higher than the theoretical capacity of graphite. The corresponding fading rate for

$CuFe_2O_4$-Fe_2O_3 electrode is about 0.02% per cycle, indicating its excellent cycling stability. It should be noted that the capacity retention of the $CuFe_2O_4$-Fe_2O_3 electrode is much better than previous reported Fe_2O_3 nanostructures including hollow nanospheres composed of ultrathin nanosheets[51], nanofibers[35] and even $CuFe_2O_4$ nanostructures[44-45, 52]. In contrast, the Fe_2O_3 nanoparticles based electrode exhibited poor cycle performance with a rapid decay of capacity from about 1100 mA h g^{-1} before 20 cycles to 500 mA h g^{-1} after 100 cycles (corresponding to a capacity loss of about 55%).

Rate capability measurement was also carried out on the $CuFe_2O_4$-Fe_2O_3 and Fe_2O_3 electrodes at various current densities (Fig. 8a). The discharge capacity was 820 mA h g^{-1} when cycled at a current density of 0.5 C for 20 cycles. When progressively increasing the current density to 1 C, 2 C and 3 C, the corresponding specific capacity values were 680 mA h g^{-1}, 559 mA h g^{-1}, 474 mA h g^{-1}, respectively. Even at the rigorously high current density of 4 C, a discharge capacity of 417 mA h g^{-1} could still be delivered, higher than that of commercial graphite. Importantly, the reversible capacity of 698 mA h g^{-1} was still retained when the current density return to 0.5 C. Additionally, the Fe_2O_3 nanoparticles based electrode demonstrated worse rate capability, as displayed in the Fig. 8a. The significantly enhanced rate performance of the self-stacked $CuFe_2O_4$-Fe_2O_3 porous nanosheets in comparison of the Fe_2O_3 nanoparticles might be closely related to their good conductivity, originated from the $CuFe_2O_4$ phase, and unique architecture. The increased conductivity was further confirmed by EIS analysis, which was carried out from 100 kHz to 0.01 Hz (Fig. S12†). The semi-circle diameter of the $CuFe_2O_4$-Fe_2O_3 porous nanosheets at the high frequency was obviously smaller than that of Fe_2O_3 nanoparticles, indicating the enhanced charge transfer. This phenomenon can be ascribed to good contact at the electrode/electrolyte interface and enhanced electrical conductivity of the overall electrode. At the low frequency region, a more vertical straight line of the $CuFe_2O_4$-Fe_2O_3 porous nanosheets compared with the Fe_2O_3 nanoparticles was evident for the fast Li^+ ion diffusion behavior of the $CuFe_2O_4$-Fe_2O_3 electrode. Thus, the above EIS result strongly verifies good electrical conductivity and large superiority of the self-stacked porous nanosheets structure as for anode materials for LIBs. Moreover, the cycling profiles of at both 1 C and 2 C rates till 240 cycles (Fig. 8b) remained at 894 mA h g^{-1} and 499 mA h g^{-1}, respectively, revealing high performance of $CuFe_2O_4$-Fe_2O_3 electrode at high current densities.

Three following reasons could be adopted to explain the excellent electrochemical properties of the self-stacked $CuFe_2O_4$-Fe_2O_3 porous nanosheets. Firstly, the highly open structure self-assembled by porous nanosheets can improve the electrochemical kinetics effectively, shorten the transport length of lithium ion and electron, offer large electrode-electrolyte interface, reduce the diffusion length and resistance of the electrolyte molecules and relax the stress caused by volume change during the charge-discharge process. Secondly, the relatively high conductive $CuFe_2O_4$ composition in the $CuFe_2O_4$-Fe_2O_3 electrode could enhance the interfacial charge transfer and lithium ion diffusion in the nanocomposite materials. Thirdly, the rich redox chemistry and the synergetic effect of copper and iron ions may also contribute to the better electrochemical performance.

4. Conclusions

In summary, uniform self-stacked $CuFe_2O_4$-Fe_2O_3 nanostructures composed of porous nanosheets had been prepared via a facile polyol-mediated route for the application as LIBs anode materials. The unique porous nanosheets combined with Fe_2O_3 and high conductive $CuFe_2O_4$ nanocrystals. Such hierarchical structured composite electrode demonstrated an excellent electrochemical performance with high capacity of 910 mA h g^{-1} at 0.5 C, good cycle stability of 0.02 % capacity loss per cycle and impressive rate capability of 417 mA h g^{-1} at 4 C. Considering its excellent electrochemical properties and simple preparation process, the as-prepared self-stacked $CuFe_2O_4$-Fe_2O_3 nanosheets might be a potential candidate for high-capacity anode material in next-generation LIBs.

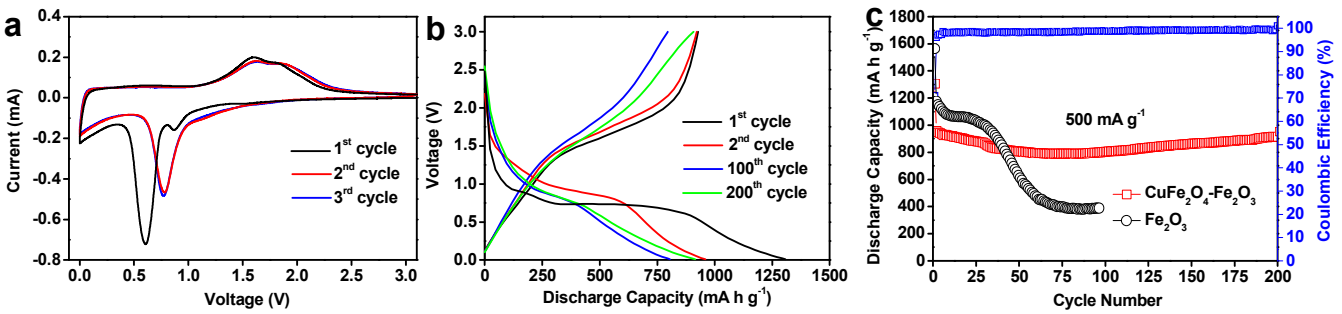

Fig. 7 (a) Cyclic voltammograms (CVs) of the $CuFe_2O_4$-Fe_2O_3 electrode at a scanning rate of 0.1 mV s^{-1}; (b) Galvanostatic charge/discharge curves of the as-prepared $CuFe_2O_4$-Fe_2O_3 nanosheets at a current density of 500 mA g^{-1}; (c) Cycling performance and the corresponding Coulombic efficiency of the self-stacked $CuFe_2O_4$-Fe_2O_3 nanosheets at a current density of 500 mA g^{-1}, □ represents the cycle performance of Fe_2O_3 nanoparticles.

Journal Name

RSCPublishing

ARTICLE

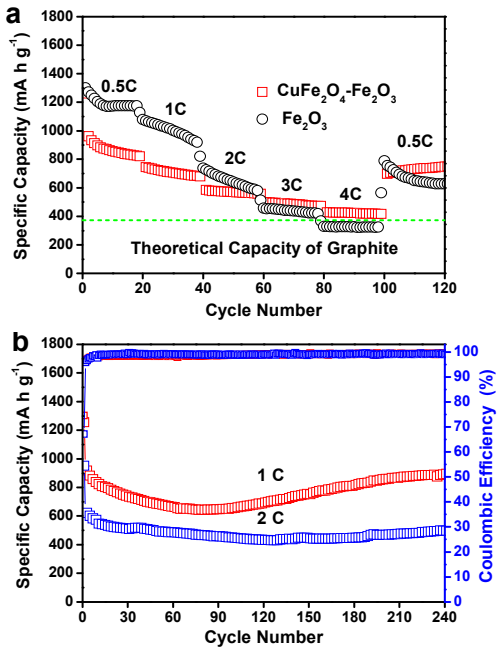

Fig. 8 (a) Rating performance of the self-stacked $CuFe_2O_4$-Fe_2O_3 nanosheet and Fe_2O_3 nanoparticle electrodes at different current densities: 0.5 C, 1 C, 2 C, 3 C, 4 C and 0.5 C (1 C = 1000 mA h g^{-1}). (b) Cycling profiles and the corresponding Coulombic efficiency of the self-stacked $CuFe_2O_4$-Fe_2O_3 nanosheet electrode at 1 C and 2 C rates.

Acknowledgements

This work was supported by Program for New Century Excellent Talents in University, Ministry of Education, China (NCET-11-0810), and Fundamental Research Funds for the Central Universities (Grant No. HIT.BRETIII.201203).

Notes and references

[a] School of Materials Science and Engineering, Harbin Institute of Technology, Harbin 150001, China.

E-mail: cy_xu@hit.edu.cn, lzhen@hit.edu.cn; Fax: +86-451-8641-3922; Tel: +86-451-8641-2133

[b] MOE Key Laboratory of Micro-system and Micro-structures Manufacturing, Harbin Institute of Technology, Harbin 150080, China

Electronic Supplementary Information (ESI) available: [XRD pattern, FT-IR and EDS result of the CuFe-glycolate precursor, EDS result, HRTEM image and SAED pattern of the calcined sample, SEM images and XRD patterns of the irregular Fe-glycolate precursor and the calcined sample and their related EIS result]. See DOI: 10.1039/b000000x/

1 J. B. Goodenough and K. S. Park, *J. Am. Chem. Soc.*, 2013, **135**, 1167-1176.
2 S. Chu and A. Majumdar, *Nature*, 2012, **488**, 294-303.
3 A. Yoshino, *Angew. Chem. Int. Ed.*, 2012, **51**, 5798-5800.
4 S. L. P. Poizot, S. Grugeon, L. Dupont and J. M. Tarascon, *Nature*, 2000, **407**, 496-499.
5 A. Banerjee, U. Singh, V. Aravindan, M. Srinivasan and S. Ogale, *Nano Energy*, 2013, **2**, 1158-1163.
6 V. Aravindan, P. Suresh Kumar, J. Sundaramurthy, W. C. Ling, S. Ramakrishna and S. Madhavi, *J. Power Sources*, 2013, **227**, 284-290.
7 J. Y. Wang, N. L. Yang, H. J. Tang, Z. H. Dong, Q. Jin, M. Yang, D. Kisailus, H. J. Zhao, Z. Y. Tang and D. Wang, *Angew. Chem. Int. Ed.*, 2013, **52**, 6417-6420.
8 B. Wang, H. B. Wu, L. Zhang and X. W. Lou, *Angew. Chem. Int. Ed.*, 2013, **52**, 4165-4168.
9 Z. X. Y. Xia, X. Dou, H. Huang, X. H. Lu, R. J Yan, Y. P Gan, W. J Zhu, J. P. Tu, W. K. Zhang, and X. Y. Tao, *ACS Nano*, 2013, **7**, 7083-7092.
10 L. L. Li, Y. Cheah, Y. W. Ko, P. Teh, G. Wee, C. L. Wong, S. J. Peng and M. Srinivasan, *J. Mater. Chem. A*, 2013, **1**, 10935-10941.
11 J. Bai, X. G. Li, G. Z. Liu, Y. T. Qian and S. L. Xiong, *Adv. Funct. Mater.*, 2014, **24**, 3012-3020.
12 C. Z. Yuan, J. Y. Li, L. R. Hou, L. H. Zhang and X. G. Zhang, *Part. Part. Syst. Char.*, 2014, **31**, 657-663.
13 Y. F. Deng, Q. M. Zhang, S. D. Tang, L. T. Zhang, S. N. Deng, Z. C. Shi and G. H. Chen, *Chem. Commun.*, 2011, **47**, 6828-6830.
14 M. V. Reddy, G. V. Subba Rao and B. V. Chowdari, *Chem. Rev.*, 2013, **113**, 5364-5457.
15 J. Cabana, L. Monconduit, D. Larcher and M. R. Palacin, *Adv. Mater.*, 2010, **22**, E170-192.
16 L. Zhang, H. B. Wu and X. W. D. Lou, *Adv. Energy Mater.*, 2014, **4**, 1300958-1300968.
17 M. V. Reddy, T. Yu, C. H. Sow, Z. X. Shen, C. T. Lim, G. V. Subba Rao and B. V. R. Chowdari, *Adv. Funct. Mater.*, 2007, **17**, 2792-2799.
18 P. G. Bruce, B. Scrosati and J. M. Tarascon, *Angew. Chem. Int. Ed.*, 2008, **47**, 2930-2946.
19 S. M. Xu, C. M. Hessel, H. Ren, R. B. Yu, Q. Jin, M. Yang, H. J. Zhao and D. Wang, *Energy Environ. Sci.*, 2014, **7**, 632-637.
20 X. W. Lou, L. A. Archer and Z. C. Yang, *Adv. Mater.*, 2008, **20**, 3987-4019.
21 Y. G. Guo, J. S. Hu and L. J. Wan, *Adv. Mater.*, 2008, **20**, 2878-2887.
22 B. Wang, J. S. Chen, H. B. Wu, Z. Wang and X. W. Lou, *J. Am. Chem. Soc.*, 2011, **133**, 17146-17148.
23 Y. H. Xu, G. Q. Jian, Y. H. Liu, Y. J. Zhu, M. R. Zachariah and C. S. Wang, *Nano Energy*, 2014, **3**, 26-35.
24 L. Zhang, H. B. Wu, S. Madhavi, H. H. Hng and X. W. Lou, *J. Am. Chem. Soc.*, 2012, **134**, 17388-17391.
25 Y. Han, Y. J. Wang, L. Li, Y. P. Wang, L. F. Jiao, H. T. Yuan and S. X. Liu, *Electrochim. Acta*, 2011, **56**, 3175-3181.
26 X. H. Ma, X. Y. Feng, C. Song, B. K. Zou, C. X. Ding, Y. Yu and C. H. Chen, *Electrochim. Acta*, 2013, **93**, 131-136.
27 X. D. Xu, R. G. Cao, S. Jeong and J. Cho, *Nano Lett.*, 2012, **12**, 4988-4991.
28 L. N. X. J. Chen, W. Y. Li and X. L. Gou *Adv. Mater.*, 2005, **17**, 582-586.
29 W. M. Zhang, X. L. Wu, J. S. Hu, Y. G. Guo and L. J. Wan, *Adv. Funct. Mater.*, 2008, **18**, 3941-3946.
30 H. S. Lim, Y. K. Sun and K. D. Suh, *J. Mater. Chem. A*, 2013, **1**, 10107-10111.
31 Z. Y. Wang, D. Y. Luan, S. Madhavi, Y. Hu and X. W. Lou, *Energy Environ. Sci.*, 2012, **5**, 5252-5256.
32 W. J. Yu, P. X. Hou, F. Li and C. Liu, *J. Mater. Chem.*, 2012, **22**, 13756-13763.
33 Y. W. Z. X. J. Zhu, S. Murali, M. D. Stoller and R. S. Ruoff, *ACS Nano*, 2012, **5**, 3333-3338.
34 S. B. Yang, Y. Sun, L. Chen, Y. Hernandez, X. L. Feng and K. Mullen, *Sci. Rep.*, 2012, **2**, 427.

35 X. Zhang, H. H. Liu, S. Petnikota, S. Ramakrishna and H. J. Fan, *J. Mater. Chem. A*, 2014.
36 Q. Li, L. W. Yin, Z. Q. Li, X. K. Wang, Y. X. Qi and J. Y. Ma, *ACS Appl. Mater. Interfaces*, 2013, **5**, 10975-10984.
37 D. Zhao, Y. Xiao, X. Wang, Q. Gao and M. H. Cao, *Nano Energy*, 2014, **7**, 124-133.
38 Y. Ma, C. L. Fang, B. Ding, G. Ji and J. Y. Lee, *Adv. Mater.*, 2013, **25**, 4646-4652.
39 Y. Qu, W. Zhou, Z. Y. Ren, S. C. Du, X. Y. Meng, G. H. Tian, K. Pan, G. F. Wang and H. G. Fu, *J. Mater. Chem.*, 2012, **22**, 16471-16476.
40 M. Y. Zhu, D. H. Meng, C. J. Wang and G. W. Diao, *ACS Appl. Mater. Interfaces*, 2013, **5**, 6030-6037.
41 G. B. Sun, B. X. Dong, M. H. Cao, B. Q. Wei and C. W. Hu, *Chem. Mater.*, 2011, **23**, 1587-1593.
42 Y. L. Zhao, L. Xu, L. Q. Mai, C. H. Han, Q. Y. An, X. Xu, X. Liu and Q. J. Zhang, *Proc. Natl. Acad. Sci. U. S. A.*, 2012, **109**, 19569-19574.
43 L. Q. Mai, F. Yang, Y. L. Zhao, X. Xu, L. Xu and Y. Z. Luo, *Nat. Commun.*, 2011, **2**, 381.
44 Z. Xing, Z. C. Ju, J. Yang, H. Y. Xu and Y. T. Qian, *Electrochim. Acta*, 2013, **102**, 51-57.
45 L. M. Jin, Y. C. Qiu, H. Deng, W. S. Li, H. Li and S. H. Yang, *Electrochim. Acta*, 2011, **56**, 9127-9132.
46 F. Han, W. C. Li, M. R. Li and A. H. Lu, *J. Mater. Chem.*, 2012, **22**, 9645-9651.
47 L. Jabbour, C. Gerbaldi, D. Chaussy, E. Zeno, S. Bodoardo and D. Beneventi, *J. Mater. Chem.*, 2010, **20**, 7344-7347.
48 H. T. Sun, G. Q. Xin, T. Hu, M. P. Yu, D. L. Shao, X. Sun and J. Lian, *Nat. Commun.*, 2014, **5**, 4526.
49 S. Laruelle, S. Grugeon, P. Poizot, M. Dollé, L. Dupont and J. M. Tarascon, *J. Electrochem. Soc.*, 2002, **149**, A627.
50 K. T. Nam, D. W. Kim, P. J. Yoo, C. Y. Chiang, N. Meethong, P. T. Hammond, Y. M. Chiang and A. M. Belcher, *Science*, 2006, **312**, 885-888.
51 J. X. Zhu, Z. Y. Yin, D. Yang, T. Sun, H. Yu, H. E. Hoster, H. H. Hng, H. Zhang and Q. Y. Yan, *Energy Environ. Sci.*, 2013, **6**, 987-993.
52 Y. Ding, Y. F. Yang and H. X. Shao, *Solid State Ionics*, 2012, **217**, 27-33.

Graphical Abstract

Uniform self-stacked $CuFe_2O_4$-Fe_2O_3 porous nanosheets with excellent electrochemical properties as anode materials for LIBs were prepared via a facile polyol-mediated route together with subsequent calcination.